Supporting Information

Dual-gradient radiative cooling aerogels with phase-change-coupled directional heat transport for adaptive thermal management

Haoran Ma[a, b], Qinxin Wang[a, b], Chen Dai[a, b], Lei Yang[a, b], Linheng He[a, b], Xiaofei Zhu[c], Ruxi Huang[d*], Sheng Cui[a, b, d*]

(a. State Key Laboratory of Materials-Oriented Chemical Engineering, College of Materials Science and Engineering, Nanjing Tech University, Nanjing, 211816, China; b. Jiangsu Collaborative Innovation Center for Advanced Inorganic Function Composites, Nanjing, 211816, China; c. Shanghai Space Propulsion Technology Research Institute, Huzhou, 313000, China; d. Institute of Electronic and Photonic Materials of Light Industry, Nanjing 210015, China.)

Corresponding author:

Ruxi Huang: hrxdz@163.com

Sheng Cui: scui@njtech.edu.cn

This Supporting Information includes:

1. Supplementary Text (Note S1-S4)

2. Supplementary Figures (Fig.S1-S20)

3. Supplementary Table (Table S1)

1. Supplementary Text

Note S1. Characterization methods

Structure, composition and properties. The microstructure of the samples was characterized using a field emission scanning electron microscope (SEM, Sigma 360, 10 kV, Germany). Pore statistics were obtained from SEM images using the image analysis software ImageJ. To evaluate the variation in apparent density of GPSBA along the gradient direction, the GPSBA monolith was sectioned into three equal-thickness slices along the thickness direction using a cutting device, and the density (ρ_0) and porosity (P) of different regions were calculated according to Eqs. (S1 and S2):

$$\rho_0 = \frac{M_{GPSBA_y}}{V_{GPSBA_y}} \tag{S1}$$

$$P = \left(1 - \frac{\rho_0}{\rho_s}\right) \times 100\% \tag{S2}$$

where M_{GPSBA_y} is the mass of the sliced GPSBA specimen at different positions, V_{GPSBA_y} is the corresponding volume, and ρ_s is the skeleton density of the aerogel composite.

The volumetric shrinkage (S_V) of GPSBA after freeze-drying was calculated according to Eq. (S3):

$$S_V = \frac{V_0 - V_1}{V_0} \times 100\% \tag{S3}$$

where V_0 is the mold volume before freeze-drying, and V_1 is the volume of GPSBA after freeze-drying.

The chemical structures of the samples were investigated using Fourier transform infrared spectroscopy (FTIR, IRSpirit-T, Japan). The crystalline structure of the

samples was characterized using an X-ray diffractometer with the following parameters: Cu Kα = 1.5406 Å, X-ray tube voltage of 35 kV, tube current of 30 mA, scanning speed of 10°/min, and scanning range of 5°-85° (XRD, Rigaku SmartLab SE, Japan). Compressive strength testing was conducted using a universal testing machine (DECCA-I, China) at a compression rate of 2 mm·min^{-1}. Water contact angles before and after hydrophobic modification were measured using an optical contact angle measuring instrument (LSA100S-T, Germany).

Thermal measurements. The melting and crystallization enthalpies of the phase-change material were measured using differential scanning calorimetry (DSC, HSC-2, China) at heating and cooling rates of 10 °C min^{-1}. The thermal conductivity of the samples was measured using the transient plane source method (DRE-2C, China), with a zeroing current of 0.002 A, a test current of 0.05 A, a temperature stability deviation of 0.02 μV, and a temperature stabilization time of 300 s. Thermal conductivity at elevated temperatures was measured with the assistance of a constant-temperature oven. The thermal rectification coefficient η was calculated according to Eq. (S4): [1, 2]

$$\eta = \left(\frac{k_f}{k_r} - 1 \right) \times 100\% = \frac{k_f - k_r}{k_r} \times 100\% \quad \text{(S4)}$$

where k_f and k_r are the effective thermal conductivities in the forward and reverse heat-transfer directions, respectively. The forward direction refers to the direction with higher effective thermal conductivity and favorable heat dissipation, while the reverse direction refers to the opposite direction. For the calculation of the thermal rectification coefficient of GPSBA, k_f represents the effective thermal conductivity measured from the dense side to the sparse side, while k_r represents that measured from the sparse side to the dense side.

Infrared thermography images were captured using an infrared thermal imager (Fluke Ti480 Pro). All temperature data were collected using a high-speed temperature data logger (CT08B) equipped with K-type thermocouples.

Spectral characterization and outdoor cooling performance. The solar reflectance spectra of the samples were measured using a UV-vis-NIR spectrophotometer equipped with a gold integrating sphere over 0.3-2.5 μm (UV-3600i Plus, Shimadzu, Japan), with a polytetrafluoroethylene (PTFE) standard white reference used as the reflectance standard. The mid-infrared reflectance and transmittance were measured using an FTIR spectrometer equipped with a gold integrating sphere over the 2.5-25 μm (Nicolet iS50, Thermo Scientific, USA). Simulated solar irradiation experiments employed a solar simulator utilizing a xenon lamp source (irradiance calibrated to 1000 $W \cdot m^{-2}$). Samples with a thickness of 1 cm were used for the simulated solar irradiation tests. The outdoor radiative cooling performance was evaluated in an open area at Nanjing Tech University using a self-assembled testing platform, where samples with dimensions of 6 × 6 × 2.5 cm were used. The sub-ambient temperature beneath the sample and the ambient temperature were simultaneously monitored by thermocouples. Solar irradiance was recorded using a solar radiometer (JD-FS, Shandong Jingdao Optoelectronic Technology Co., Ltd., China), and meteorological parameters such as wind speed and relative humidity were recorded using a portable meteorological instrument (OWM5500, Fujian Lilliput Optoelectronics Technology Co., Ltd., China).

Thermal cycling stability test. The thermal cycling stability of the samples was tested using a high-low-temperature alternating test chamber (GOJS-010, China). Samples with dimensions of 3.3 × 3.3 × 1.0 cm were placed in the chamber and subjected to repeated heating–cooling cycles between 0 and 60 °C. During each cycle, the samples were maintained at 0 °C and 60 °C for 1 h, respectively, to simulate repeated low- and high-temperature fluctuations and the melting–crystallization process of the encapsulated PCM. After thermal cycling, the samples were naturally equilibrated to room temperature before subsequent characterization.

Note S2. GPSBA asymmetric heat transfer simulation

Numerical simulation of asymmetric thermal conduction behavior was performed using COMSOL Multiphysics to investigate the contribution of the gradient pore structure to

directional heat conduction. To simplify the analysis, a two-dimensional heat-conduction model with a computational domain of 1 mm × 1 mm was established. The aerogel skeleton was treated as a continuous solid matrix, while the pores were represented as circular voids. The gradient architecture was approximated by a three-layer pore-size distribution, and the pore parameters of each layer were determined from cross-sectional SEM images using ImageJ. This simulation focused on the structural origin of directional heat conduction; therefore, each layer was described using an effective thermal-conduction parameter to compare the forward and reverse heat-transfer tendencies under identical boundary conditions. Two opposite thermal-driving cases ("forward" and "reverse") were constructed by applying boundary conditions. For forward heat transfer, the bottom and top boundaries were set to 343.15 K and 293.15 K, respectively; for reverse heat transfer, the hot and cold boundaries were swapped while all other conditions remained unchanged. All remaining boundaries were set as adiabatic to eliminate lateral heat dissipation.

Note S3. Calculation of solar weighted reflectance and atmospheric window emissivity

Based on the measured spectral reflectance and emissivity, the solar-weighted average reflectance $\bar{R}_{solar}$ and the average emissivity in the atmospheric window band $\bar{\varepsilon}_{IR}$ were calculated using Eqs. (S5 and S6):[3, 4]

$$\bar{R}_{solar} = \frac{\int_{0.3\,\mu m}^{2.5\,\mu m} I_{AM\,1.5}(\lambda) R(\lambda) d\lambda}{\int_{0.3\,\mu m}^{2.5\,\mu m} I_{AM\,1.5}(\lambda) d\lambda} \quad \text{(S5)}$$

$$\bar{\varepsilon}_{IR} = \frac{\int_{8\,\mu m}^{13\,\mu m} I_{BB}(\lambda, T_a) \varepsilon(\lambda) d\lambda}{\int_{8\,\mu m}^{13\,\mu m} I_{BB}(\lambda, T_a) d\lambda} \quad \text{(S6)}$$

where λ is the wavelength; $I_{\mathrm{AM1.5}}(\lambda)$ is the AM1.5 global solar spectral irradiance given in the ASTM G173 standard, $R(\lambda)$ is the spectral reflectance of the sample at wavelength λ (0.3-2.5 μm), and $I_{\mathrm{BB}}(\lambda,T_a)$ is the spectral radiance of a blackbody at wavelength λ and ambient temperature T_a, which can be obtained from Planck's law as Eq. (S7):

$$I_{BB}(\lambda,T) = \frac{2hc^2}{\lambda^5} \frac{1}{e^{hc/(\lambda k_B T)} - 1} \tag{S7}$$

Here, h is Planck's constant (6.626×10^{-34} J·s), c is the speed of light in vacuum (2.998×10^{8} m·s^{-1}), and k_B is the Boltzmann constant (1.381×10^{-23} J·K^{-1}). In this work, the ambient temperature was set to T_a = 298 K.

$\varepsilon(\lambda)$ is the spectral emissivity of the sample in the atmospheric window band (8-13 μm). According to Kirchhoff's law, under thermal equilibrium, the emissivity at a given wavelength equals the absorptivity, which can be expressed as Eq. (S8):

$$\varepsilon(\lambda) = A(\lambda) = 1 - R(\lambda) - T(\lambda) \tag{S8}$$

where $T(\lambda)$ is the spectral transmittance of the sample at wavelength λ.

Note S4. Calculation of theoretical net cooling power

To quantitatively evaluate the cooling capability of radiative-cooling aerogels under typical meteorological conditions, an energy-balance model was established by considering the major energy exchange processes between the sample and the environment. The net cooling power per unit area, P_{net}, was calculated using Eqs. (S9 and S10):[5, 6]

$$P_{net}(T) = P_{rad}(T) - P_{atm}(T_{amb}) - P_{sun} - P_{nonrad} \tag{S9}$$

When the regulation effect of the BN@PCM phase-change unit is considered, the net

cooling power can be modified as:

$$P_{net}(T) = P_{rad}(T) - P_{atm}(T_{amb}) - P_{sun} - P_{nonrad} + P_{PCM} \quad \text{(S10)}$$

where T is the sample temperature and T_{amb} is the ambient temperature. $P_{rad}(T)$ is the radiative power emitted by the sample to outer space, $P_{atm}(T_{amb})$ is the atmospheric back-radiation absorbed by the sample, P_{sun} is the absorbed solar irradiance power in the solar band, P_{nonrad} is the non-radiative heat exchange power including conduction and convection, and P_{PCM} is the equivalent latent-heat power associated with heat absorption/release of the phase-change unit during phase transition. These terms were calculated by Eq. (S11-S15):[7-11]

$$P_{rad}(T) = \int d\Omega cos\theta \int_0^{\infty} d\lambda I_{BB}(T,\lambda)\varepsilon(\lambda,\theta) \quad \text{(S11)}$$

where Ω is the solid angle of the upper hemisphere, and θ is the angle between the radiation direction and the surface normal of the sample. $\int d\Omega = 2\pi \int_0^{\pi/2} sin\theta \, d\theta$ represents the integration over all outgoing directions in the hemispherical space. $\varepsilon(\lambda,\theta)$ is the angular spectral emissivity of the sample at wavelength λ and direction θ. In practical calculations, the sample is assumed to approximately satisfy Lambertian behavior in the mid-infrared band, i.e., $\varepsilon(\lambda,\theta) \approx \varepsilon(\lambda)$, so the angular integration can be simplified into a constant factor, and the wavelength integration is performed over 2.5-25 μm to obtain the radiative heat flux per unit area.

The atmospheric back-radiation absorbed by the sample, P_{atm}, can be expressed as:

$$P_{atm}(T_{amb}) = \int d\Omega cos\theta \int_0^{\infty} d\lambda I_{BB}(T_{amb},\lambda)\varepsilon(\lambda,\theta)\varepsilon_{atm}(\lambda,\theta) \quad \text{(S12)}$$

where $\varepsilon_{atm}(\lambda,\theta) = 1 - \tau(\lambda)^{1/cos\theta}$ is the effective atmospheric emissivity at the

corresponding wavelength and direction, which is generally obtained from the zenith atmospheric transmittance $\tau(\lambda)$.

The absorbed solar irradiance power of the sample, P_{sun}, can be expressed as:

$$P_{sun} = \int_0^\infty d\lambda \varepsilon(\lambda,\theta_{sun}) I_{AM1.5}(\lambda) \tag{S13}$$

P_{nonrad} mainly includes natural convection and parasitic conduction between the sample and the environment, and can be written as:

$$P_{nonrad}(T,T_{amb}) = h(T_{amb} - T) \tag{S14}$$

where h is the non-radiative heat transfer coefficient. In the calculations, h was set to 0, 3, 6, 9, and 12 $W \cdot m^{-2} \cdot K^{-1}$.

Since GPSBA incorporates the BN@PCM phase-change unit, the equivalent "cooling power" associated with latent heat, P_{PCM}, is further introduced. Over a given operating time t, the average power corresponding to heat absorbed or released during the phase transition of BN@PCM can be expressed as:

$$P_{PCM} = \frac{\Delta H \times M}{t \times A} \tag{S15}$$

where ΔH is the phase-change enthalpy of BN@PCM (taken as 150 $J \cdot g^{-1}$ in this work), M is the total mass of BN@PCM in the sample (4.5 g in the field test), A is the radiative area of the sample, and t is the effective operating time associated with the phase-change process, which was set to 8 h for both daytime and nighttime in this work. During daytime, when the sample temperature is higher than the phase-change temperature of BN@PCM, BN@PCM melts and absorbs heat, leading to $P_{PCM} > 0$, which contributes positively to P_{net}. At night or during ambient cooling, BN@PCM solidifies and releases latent heat, resulting in $P_{PCM} < 0$, which reduces the

instantaneous net cooling power under the energy-conservation framework, while being beneficial for suppressing overcooling of the system[12].

2. Supplementary Figures

Commercial microencapsulated phase-change materials (PCM) with n-octadecane as the core and PMMA as the shell were used in this work. To endow the microcapsules with enhanced thermal conductivity and improved spectral regulation without compromising their structural integrity, a tetrabutyl titanate (TT)-mediated h-BN surface-coating strategy was employed to prepare BN@PCM. Specifically, h-BN nanosheets were first exfoliated and dispersed in a water/alcohol mixture to expose additional surface hydroxyl sites. Subsequently, a prescribed amount of PCM particles was added and uniformly dispersed, followed by gentle stirring in a water bath at 50 °C. TT was then introduced dropwise, allowing in situ hydrolysis in the mixed system to form a titanol-rich interlayer (-$Ti(OH)_x$). On the one hand, this interlayer underwent condensation with the hydroxyl groups (-OH) on the h-BN surface to form Ti-O-BN bonds, on the other hand, it reacted with the ester groups (-COOR) of the PMMA shell to generate stable Ti-O-C bonds, thereby enabling uniform coating of h-BN on the outer surface of the microcapsules. As shown in Fig. S1(a, b), pristine PCM particles are nearly spherical with a smooth and dense surface, whereas BN@PCM treated with TT/BN is covered by abundant h-BN nanosheets, forming a rough “scaly” outer layer. The FT-IR spectra in Fig. S2 confirm the chemical coupling between BN and PCM, the PCM sample exhibits a characteristic C-O-C stretching band of the PMMA shell at ~1150 cm^{-1}, while the BN sample shows a typical B-N stretching vibration at ~760 cm^{-1} and a broad -OH absorption band at ~3430 cm^{-1}. In BN@PCM, these bands coexist with an accompanying change in the C-O-C band intensity, indicating the condensation reaction between the titanate-derived species and the PMMA shell. This confirms the effective chemical coupling between BN and PCM. The XRD patterns in Fig. S3 further support this conclusion. PCM shows only a broad and weak amorphous halo at around $2\theta \approx 20°$, whereas BN displays a set of sharp characteristic diffraction peaks; BN@PCM presents both the BN crystalline peaks and the PCM broad halo with negligible peak shifts, suggesting that BN is loaded onto the capsule shell as a thin layer while maintaining its crystalline structure. To directly verify the interfacial bonding

structure, XPS analysis was performed on BN@PCM (Fig. S4). The survey spectrum confirms the coexistence of B, N, C, O, and Ti elements, indicating the simultaneous presence of h-BN, the PMMA shell, and titanate-derived species. In the high-resolution Ti 2p spectrum, the peaks at 458.56 and 464.24 eV correspond to Ti $2p_{3/2}$ and Ti $2p_{1/2}$, respectively, demonstrating the formation of Ti-O coordination environments. The O 1s spectrum can be deconvoluted into three components at 530.05, 532.01, and 533.58 eV, which are assigned to Ti-O, Ti-O-C/Ti-O-BN, and C-O bonds, respectively. In addition, the C 1s spectrum shows peaks at 284.80, 286.21, and 288.82 eV, corresponding to C-C/C-H, C-O/C-O-Ti, and O-C=O bonds, respectively. These XPS results provide direct chemical-state evidence for the formation of Ti-O-C and Ti-O-BN interfacial linkages, confirming the TT-mediated molecular-bridge effect between h-BN and the PMMA shell of PCM. The functional modification strategy of BN@PCM provides the PCM microcapsules with a continuous phonon-transport channel that is intimately coupled to the capsule shell, thereby accelerating the thermal response of the phase-change units and improving the uniformity of the temperature field[13, 14]. Meanwhile, the introduction of BN nanosheets with a high refractive index and a wide bandgap creates additional interfacial sites and optical tunability, thereby enhancing near-infrared scattering and mid-infrared emission for subsequent radiative-cooling applications.

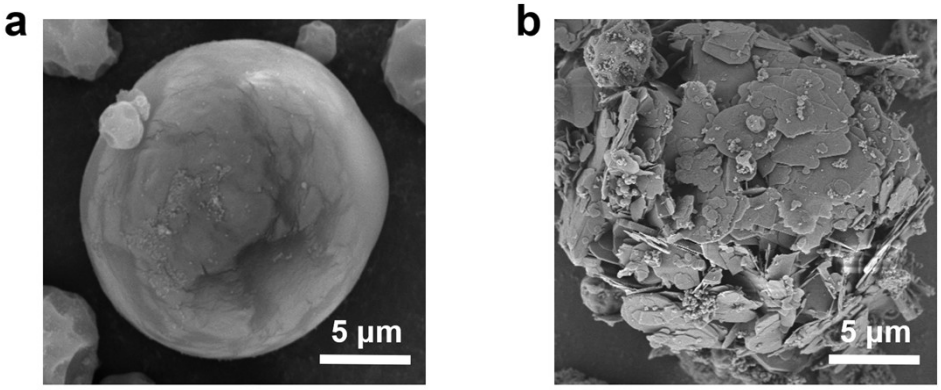

Fig. S1 (a) SEM images of PCM particles. (b) SEM images of BN@PCM particles.

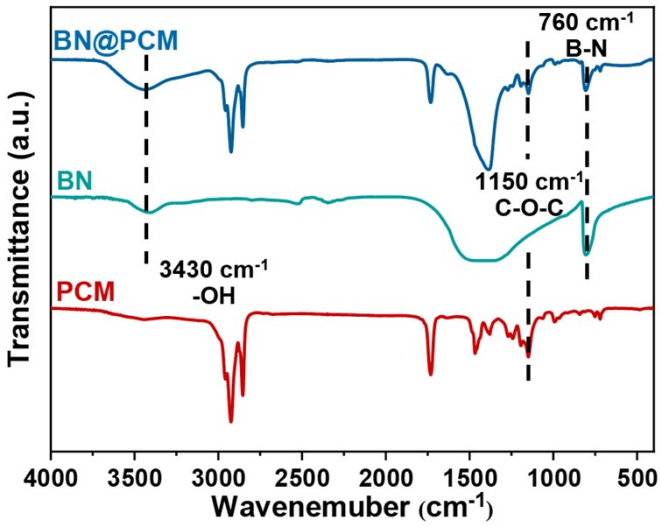

Fig. S2 FT-IR spectra of PCM, BN and BN@PCM.

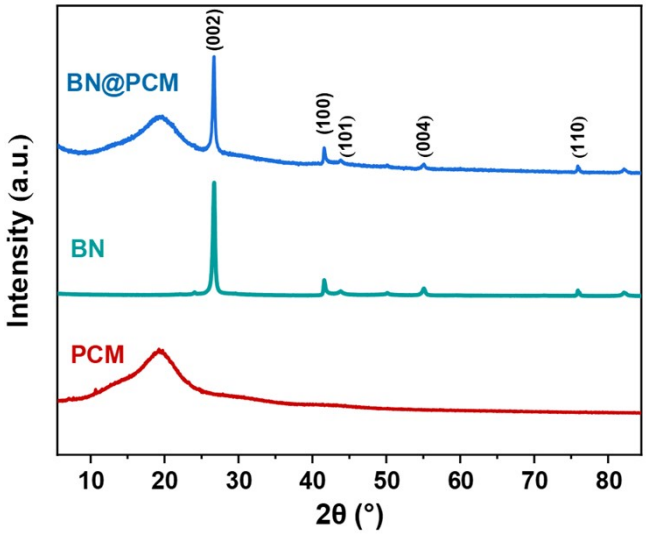

Fig. S3 XRD patterns of PCM, BN and BN@PCM.

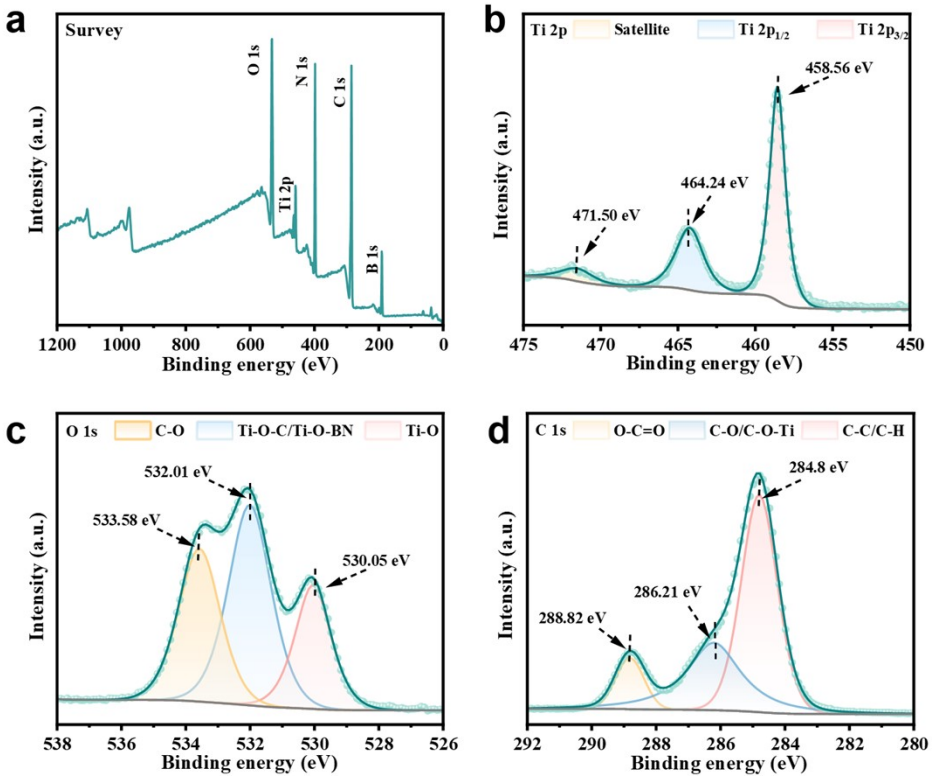

Fig. S4 (a) XPS survey spectrum of BN@PCM; high-resolution XPS spectra of (b) Ti 2p, (c) O 1s, and (d) C 1s.

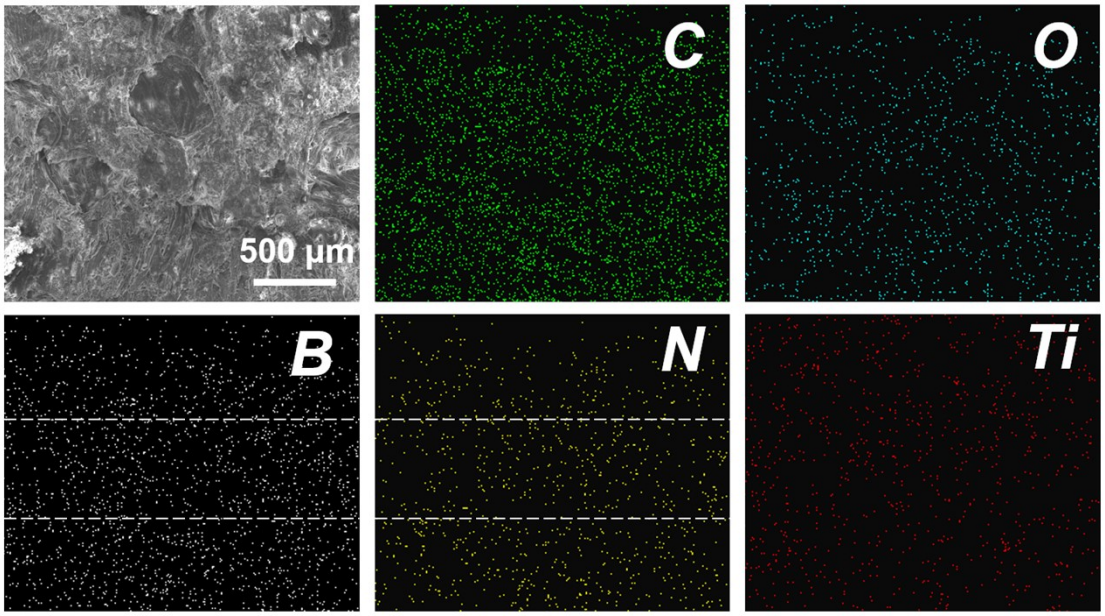

Fig. S5 SEM-EDS image and elemental distribution of the GPSBA cross-section.

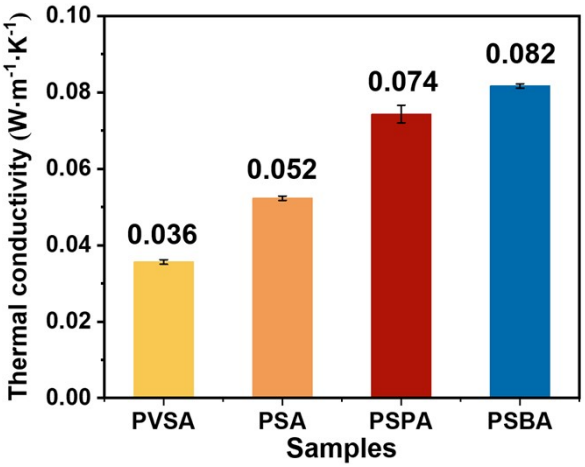

Fig. S6 Thermal conductivity at room temperature for PVSA, PSA, PSPA and PSBA.

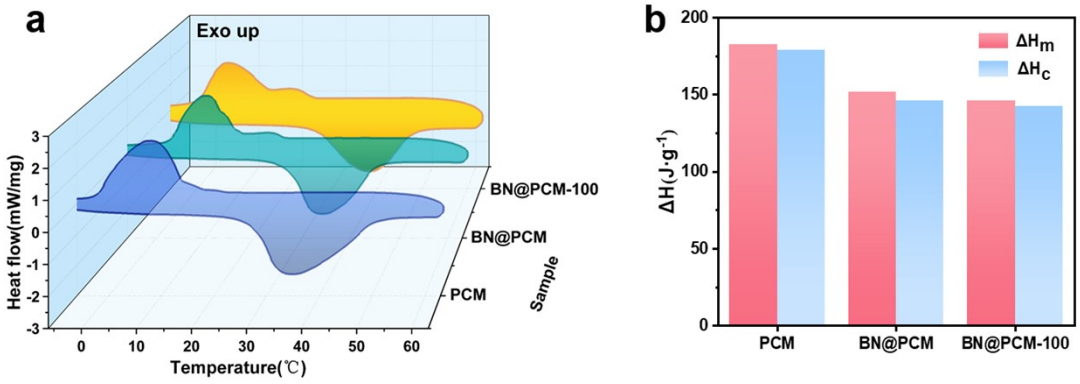

Fig. S7 (a) DSC curves for PCM, BN@PCM, and BN@PCM after 100 cycles. (b) Melting enthalpy (ΔH_m) and crystallization enthalpy (ΔH_f) of PCM, BN@PCM, and BN@PCM after 100 cycles.

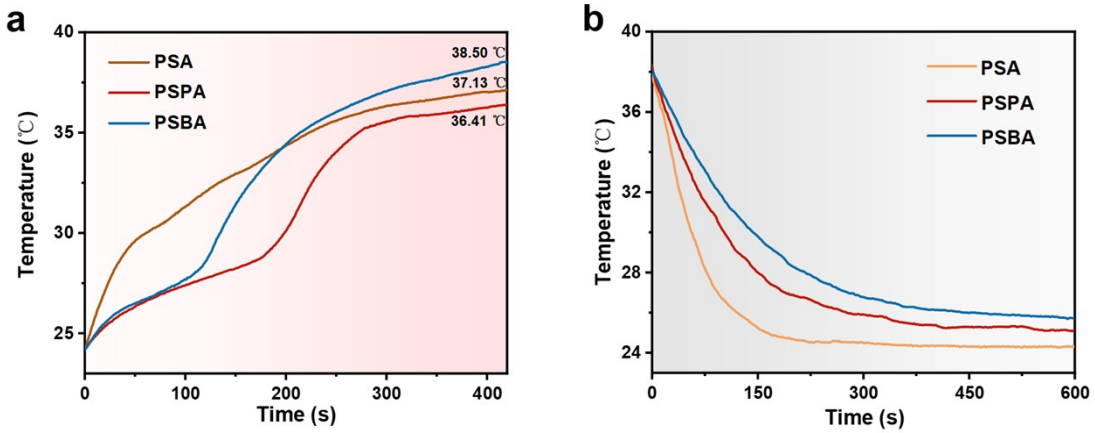

Fig. S8 (a) Surface temperatures of PSA, PSPA and PSBA during heating tests on a 60°C hot stage. (b) Surface temperatures of PSA, PSPA and PSBA during natural cooling processes.

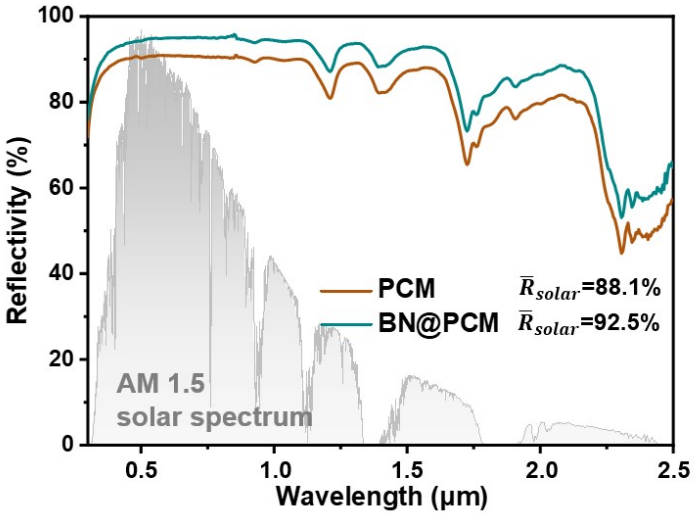

Fig. S9 Reflectance of PCM and BN@PCM microcapsules in the solar spectrum at wavelengths of 300 to 2500 nm.

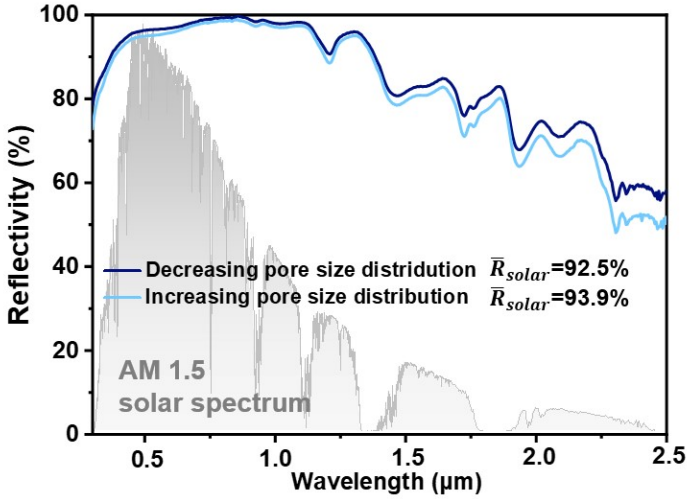

Fig. S10 Reflectance of sunlight in the 300 to 2500 nm spectral range on both sides of the GPSBA.

Fig. S11 Photograph of a homemade outdoor radiative cooling performance testing apparatus.

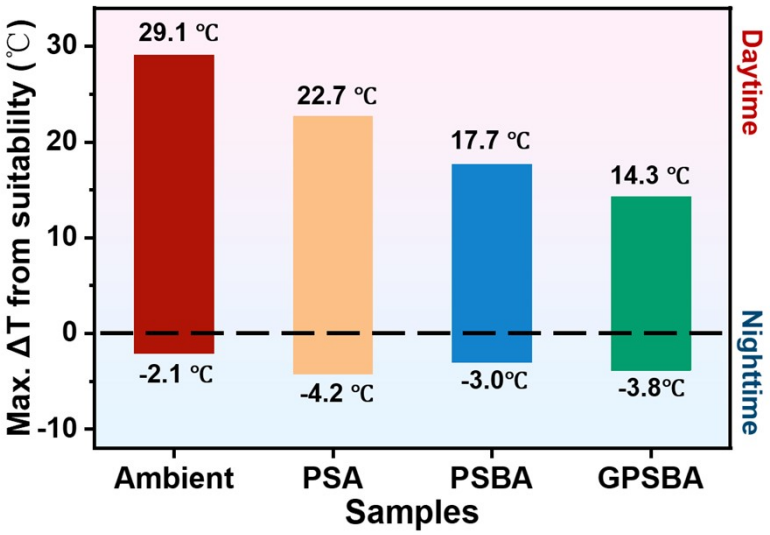

Fig. S12 The difference between the daily temperature fluctuations of each sample and the optimal temperature of 25°C within the enclosed space.

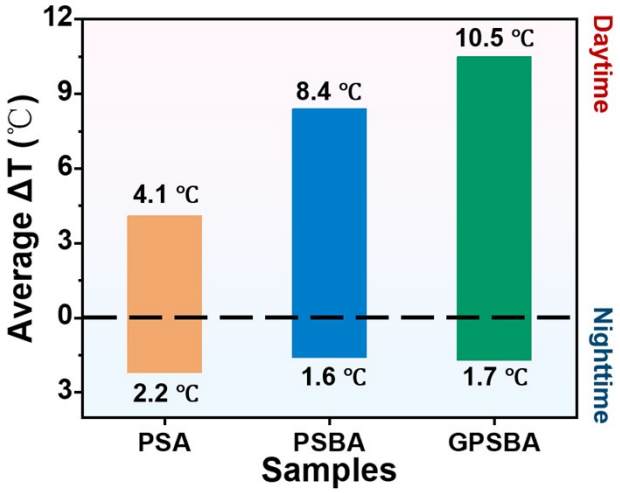

Fig. S13 Average temperature decrease for each sample during midday and nighttime.

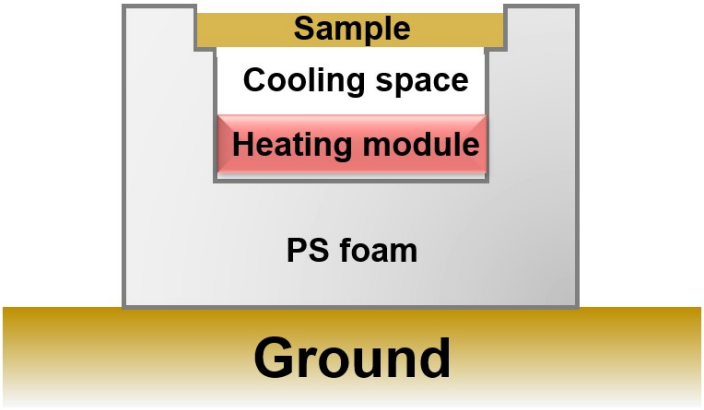

Fig. S14 Schematic diagram of a self-constructed radiative cooling performance testing apparatus incorporating an internal heating unit.

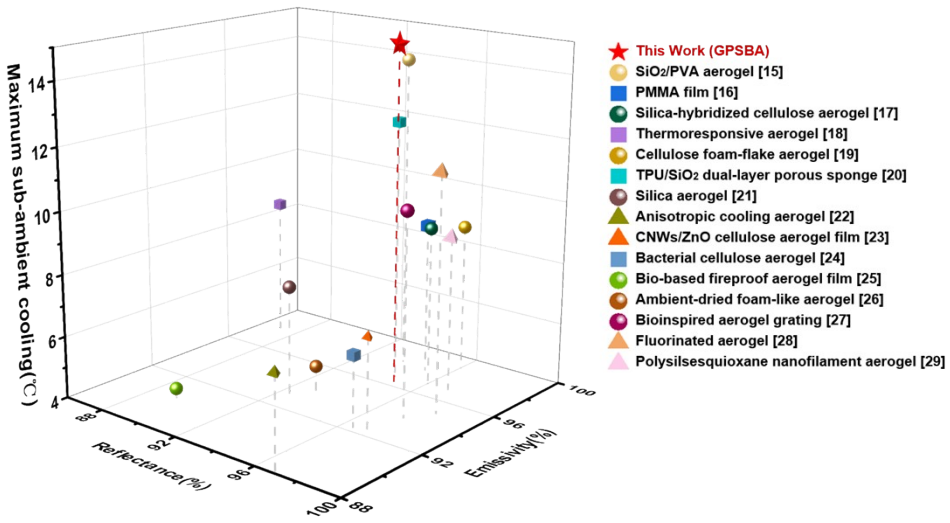

Fig. S15 Performance comparison of GPSBA with reported porous radiative-cooling materials.

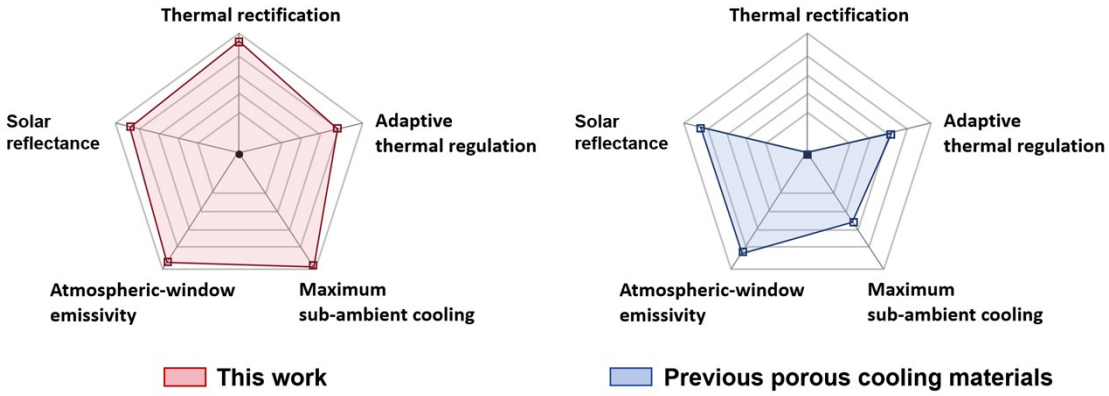

Fig. S16 Comprehensive thermal-management performance comparison between the dual-gradient aerogel developed in this work and previously reported porous radiative-cooling materials.

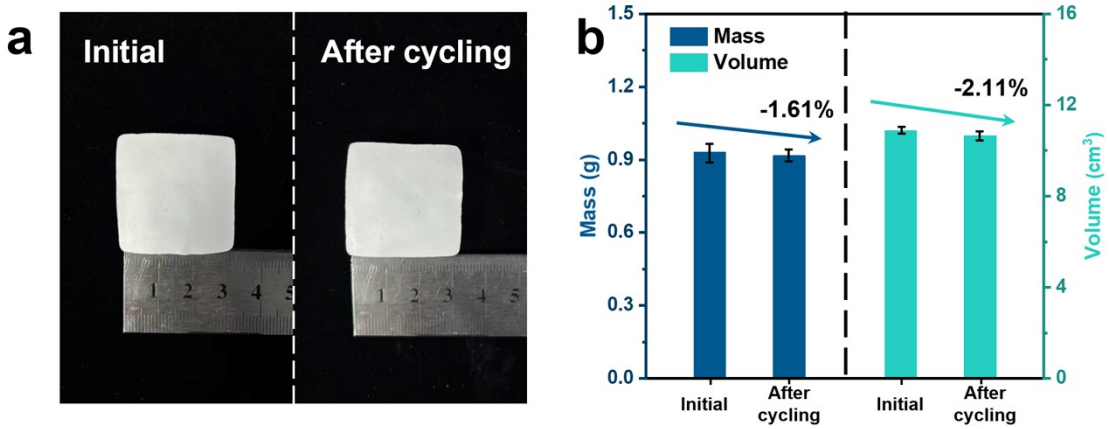

Fig. S17 (a) Photographs of GPSBA in the initial state and after heating–cooling cycles; (b) mass and volume changes of GPSBA before and after heating–cooling cycles.

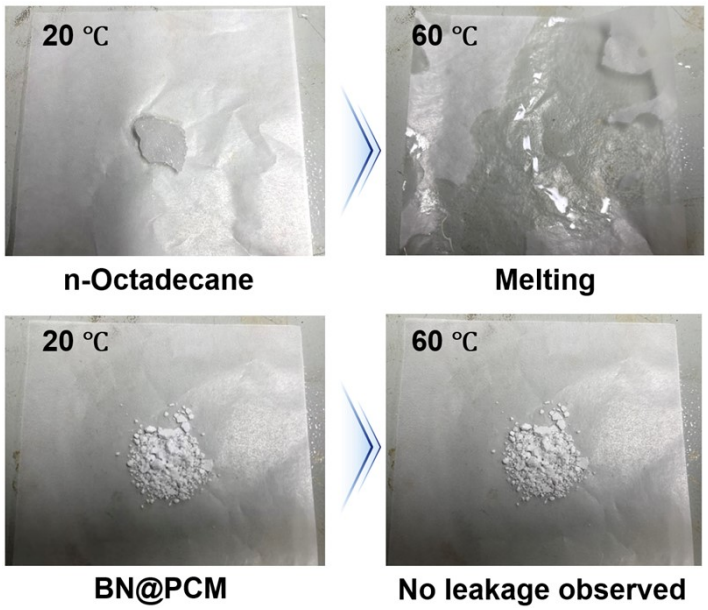

Fig. S18 Leakage resistance comparison of n-octadecane and BN@PCM.

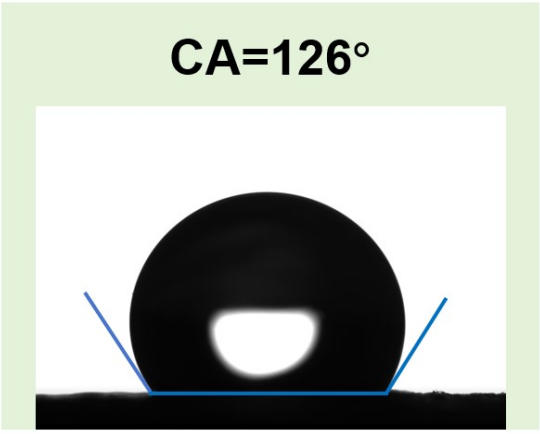

Fig. S19 Water contact angle of GPSBA after repeated heating-cooling cycles.

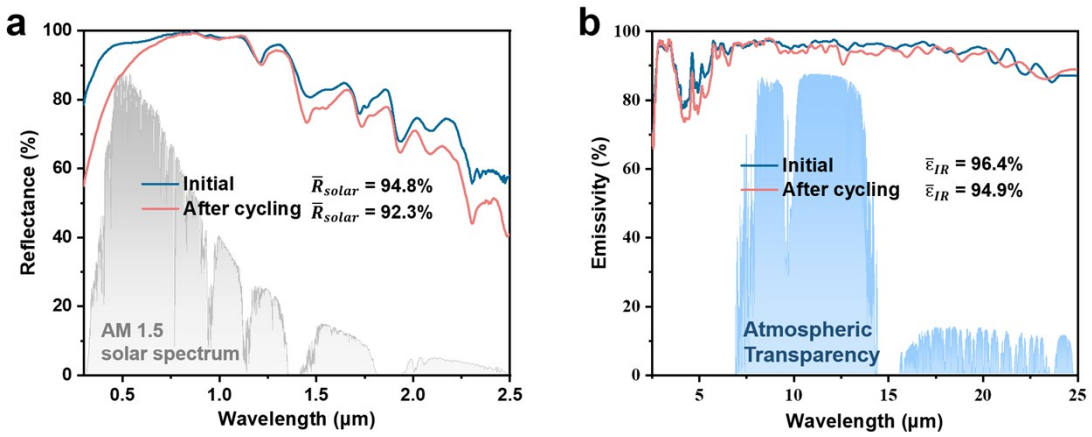

Fig. S20 (a) Solar reflectance spectra of GPSBA before and after heating-cooling cycles; (b) infrared emissivity spectra of GPSBA before and after heating-cooling cycles.

3. Supplementary Table

Table S1 Formulations and freezing protocols of GPSBA and control aerogels

sample	H_2O (wt%)	PVA(wt%)	SA(wt%)	PCM(wt%)	BN@PCM(wt%)	Freezing protocol
PVSA	94	4.5	1.5	/	/	Static freezing
PSA	94	4.5	1.5	/	/	Directional freezing
PSPA	88	4.5	1.5	6	/	Directional freezing
PSBA	88	4.5	1.5	/	6	Directional freezing
GPSBA	84/88/92	6/4.5/3	2/1.5/1	/	8/6/4	Multistage directional freezing

Note: For GPSBA, the values correspond to the bottom /middle /top layers, respectively. The middle and top precursor units are obtained by diluting the mother liquor to 75% and 50% of the initial concentration.

References

[1] Jiang C, Yang X, He X, et al. Janus particles stabilized asymmetric porous composites for thermal rectification[J]. Nature Communications, 2025, 16(1): 5650.

[2] Qi L, Cai W, Cui T, et al. Anisotropic radiative cooling dynamics enabling efficient thermal hazard mitigation via hierarchically engineered thermal diodes[J]. Advanced Functional Materials, 2026, 36(2): e08101.

[3] XIONG L, WEI Y, CHEN C, et al. Thin lamellar films with enhanced mechanical properties for durable radiative cooling [J]. Nature Communications, 2023, 14(1): 6129.

[4] MA Z, FENG Y, SONG A Y, et al. A Scalable, Durable, Fire-Safe All-Day Passive Radiative Cooling Coating for Sustainable Buildings [J]. Advanced Functional Materials, 2025: e17278.

[5] BU K, HUANG X, LI X, et al. Consistent assessment of the cooling performance of radiative cooling materials [J]. Advanced Functional Materials, 2023, 33(51): 2307191.

[6] HUANG K, HUANG Z, DU Y, et al. Advances in radiative cooling materials for building energy efficiency: a decade of progress [J]. Journal of Materials Chemistry A, 2024, 12(42): 28682-710.

[7] LI D, LIU X, LI W, et al. Scalable and hierarchically designed polymer film as a selective thermal emitter for high-performance all-day radiative cooling [J]. Nature Nanotechnology, 2021, 16(2): 153-8.

[8] Du Q, Yang M, Sun H, et al. A Leakage-Proof Wrapped Cooler with Daytime Radiative Cooling and Efficient Thermal-Shock Resistance for Outdoor Electronics Thermal Management[J]. Advanced Functional Materials, 2025, 35(34): 2500131.

[9] CHENG Z, HAN H, WANG F, et al. Efficient radiative cooling coating with biomimetic human skin wrinkle structure [J]. Nano Energy, 2021, 89: 106377.

[10] SHAN X, LIU L, WU Y, et al. Aerogel-functionalized thermoplastic polyurethane as waterproof, breathable freestanding films and coatings for passive daytime radiative cooling [J]. Advanced Science, 2022, 9(20): 2201190.

[11] JIANG W, ZHU T, CHEN J, et al. Phase change foam with temperature-adaptive radiative cooling feature for all-day building energy saving [J]. Chemical Engineering Journal, 2024, 502: 157862.

[12] WANG S, WU M, HAN H, et al. Regulating cold energy from the universe by bifunctional phase change materials for sustainable cooling [J]. Advanced Energy Materials, 2024, 14(45): 2402667.

[13] PENG Y, DONG J, GU Y, et al. Smart temperature-adaptive thermal regulation textiles integrating passive radiative cooling and reversible heat storage [J]. Nano Energy, 2024, 131: 110311.

[14] LI S-Z, ZHOU Y-C, WANG L-N, et al. Flexible composite phase change materials with enhanced thermal conductivity and mechanical performance for thermal management [J]. Journal of Materials Chemistry A, 2023, 11(35): 18832-18842.

[15] Ma C Q, Xue C H, Fan W, et al. Synchronous radiative cooling and thermal insulation in SiO2/poly (vinyl alcohol) composite aerogel for energy savings in building thermal management[J]. ACS Sustainable Chemistry & Engineering, 2024, 12(14): 5695-5704.

[16] Wang T, Wu Y, Shi L, et al. A structural polymer for highly efficient all-day passive radiative cooling[J]. Nature communications, 2021, 12(1): 365.

[17] Liu Y, Bu X, Liu R, et al. Construction of robust silica-hybridized cellulose aerogels integrating passive radiative cooling and thermal insulation for year-round building energy saving[J]. Chemical Engineering Journal, 2024, 481: 148780.

[18] Liang Y, Zhang X, Wang J, et al. Adaptive Radiative Cooling and Thermal Insulation Enabled by Thermoresponsive Cholesteric Liquid Crystal Aerogels[J]. Journal of Materials Chemistry C, 2026.

[19] Chen F, Bi H, Wang C, et al. Sustainable Cellulose-Based Aerogels with a Hierarchical "Foam-Flake" Structure for Ultrahigh Emissivity Radiative Cooling[J]. Advanced Functional Materials, 2026: e28466.

[20] Qu Y Y, Xue C H, Liu B Y, et al. Superhydrophobic thermoplastic polyurethane/SiO2 sponge with dual-layer porous structure for summer radiative cooling and winter thermal insulation[J]. Journal of Materials Science, 2024, 59(42): 20107-20120.

[21] Ma B, Cheng Y, Hu P, et al. Passive daytime radiative cooling of silica aerogels[J]. Nanomaterials, 2023, 13(3): 467.

[22] Chan K Y, Shen X, Yang J, et al. Scalable anisotropic cooling aerogels by additive freeze-casting[J]. Nature communications, 2022, 13(1): 5553.

[23] Cai C, Sun Y, Chen Y, et al. Large scalable, ultrathin and self-cleaning cellulose aerogel film for daytime radiative cooling[J]. Journal of Bioresources and Bioproducts, 2023, 8(4): 421-429.

[24] Qu J, Xue J, Qi Y, et al. Sustainable silylated bacterial cellulose/MgAl-LDH composite aerogel integrating radiative cooling and thermal insulation for building energy saving[J]. International Journal of Biological Macromolecules, 2025, 334: 149221.

[25] Cai W, Lin B, Qi L, et al. Bio-based and fireproof radiative cooling aerogel film: Achieving higher sustainability and safety[J]. Chemical Engineering Journal, 2024, 488: 150784.

[26] Peng Z C, Zeng F R, Zeng Z W, et al. Scalable low-carbon ambient-dried foam-like aerogels for radiative cooling with extreme environmental resistance[J]. Advanced Materials, 2025, 37(35): 2505224.

[27] Cai C, Chen W, Wei Z, et al. Bioinspired "aerogel grating" with metasurfaces for durable daytime radiative cooling for year-round energy savings[J]. Nano Energy, 2023, 114: 108625.

[28] Wang Q, Fan J, Zheng Z, et al. Flexible passive daytime radiative cooling aerogel with outstanding amphiphobic monolith properties[J]. ACS Applied Energy Materials, 2024, 7(15): 6230-6235.

[29] Xu J, Chen K, Maturilli A, et al. Biomass-derived polysilsesquioxane nanofilament reinforced porous aerogel for durable passive radiative cooling across all day and weather conditions[J]. ACS nano, 2025, 19(44): 38395-38407.